Chaos, Solitons and Fractals 199 (2025) 116579

Contents lists available at ScienceDirect

Chaos, Solitons and Fractals

journal homepage: www.elsevier.com/locate/chaos

Review article

Recent outcomes in time-dependent driven polymer translocation: A brief review

A. Sáinz-Agost, F. Falo, A. Fiasconaro *

Dpto. de Física de la Materia Condensada, Universidad de Zaragoza, Zaragoza, 50009, Spain
Instituto de Biocomputación y Física de Sistemas Complejos, Universidad de Zaragoza, Zaragoza, 50018, Spain

ARTICLE INFO

Keywords:
Polymer translocation
Polymer physics
Langevin equation
Sequencing methods

ABSTRACT

Translocation processes have long been a topic of interest in the scientific community due to their involvement in fundamental biological functions, as well as applications in nanotechnology. This review explores the translocation of coarse-grained polymer chains through extended pores, focusing on the results obtained under time dependent drivings applied either within the cavity (active pore) or at the polymer's extremities (end-pulled). Additionally, the review discusses the potential application of polymer translocation in identifying protein secondary structures, and in this context presents promising preliminary outcomes.

1. Introduction

Translocation process is a fundamental phenomenon at every scale in biology. In essence, it consists of the dynamics of a translocating body (be it molecule, polymer, protein or others) that moves from an initial zone, called *cis*, to a new region, named *trans*, separated by a porous membrane. In particular, the study of translocation processes usually pertains to the description of the interaction of the pore and the membrane with the translocating object.

The relevance of these processes, in both technological and biological contexts, has made translocation a field of interest for soft-matter physics. Examples are the transportation of DNA/RNA and proteins through different membranes [1], viral DNA injection [2] or protease-leaded translocation for targeted degradation [3], in the biological field, and DNA sequencing through either biological or artificial nanopores [4], biosensing [5,6] and drug delivery [7] in the realm of nanotechnology.

Translocation dynamics can be divided in two main categories depending on the underlying driving force applied to the chain: *passive* translocation, which refers to the movement of translocating elements driven by thermal mechanisms – such as diffusion –, concentration gradients or favorable entropy changes without involving extrinsic energy sources, and *active* translocation, where energy (usually in the form of ATP in biological porous or external fields in nanotechnological devices) is used to move molecules. In the latter, forces can be applied either inside the propagating channel, or directly pulling the molecule from one of its edges.

The models involved in the translocation process have increased in complexity over time. Initial theoretical studies focused on polymer–membrane interactions, often considering ideal chains and pores of negligible lengths [8–10]. In parallel, experimental work was developed based on the application of constant forces to the translocating molecule [11,12], where the pore remained a passive channel that permits the passage of the molecule between the two sides of a membrane [13]. In some studies, the force was applied via an electric field to a chain of DNA [1,12,14]. This voltage-regulated translocation, in combination with the presence of ions in the medium, has permitted the possibility of determining the DNA sequence through the changes in the current traversing the pore; when a given nucleotide is translocating it reduces the space available for the ions to cross the pore, thus reducing the overall current. Each nucleotide has a different characteristic size, which leads to a corresponding current value, allowing the determination of the specific sequence [1]. Interest in this particular application culminated with the design of a simple, fast, and reliable for DNA sequencing technique [15].

Since then more complicated approaches to translocation have been taken, aiming to mimic the properties of translocation phenomena observed in biological systems. An example is the introduction of ratchet-like potentials to simulate the irreversible character of the driving mechanism [16,17], describing the behavior of different molecular machines.

In the same line of thinking and in accordance with the time-dependent activity of multiple molecular machines, active pore drivings

* Corresponding author.
E-mail address: afiascon@unizar.es (A. Fiasconaro).

https://doi.org/10.1016/j.chaos.2025.116579
Received 6 February 2025; Received in revised form 2 April 2025; Accepted 6 May 2025
Available online 11 June 2025

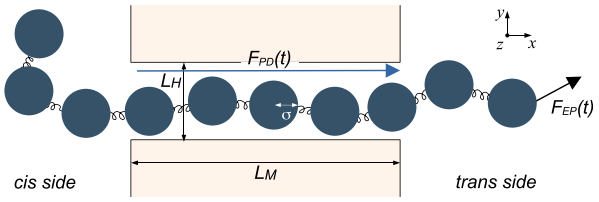

Fig. 1. Scheme of the model for polymer translocation. The two forces represent the different modes of driving studied in this review: $F_{PD}(t)$ is the force of the pore-driven translocation, applied to the monomers inside the channel and $F_{EP}(t)$ is the force of the end-pulled translocation, applied onto the end of the chain.

have also been largely studied over the last decade [16,18–23]. Differences between them relate to the time dependency of the driving itself, ranging from sinusoidal waves [18,19] to stochastic random telegraph noises (RTN) [23] or dichotomous ATP-based noises, motivated by molecular motors [16,24,25].

Regarding the modeling of the pores themselves, *i.e.* based on their dimensions, we distinguish point-like [26] or spatially extended, so more realistic, pores [19].

There are multiple methods available for the application of the driving force. For this review, as also mentioned above, we will focus on two of these approaches: *active pore* translocation [19,27,28], in which the driving force is applied in the space inside the channel, and *end-pulled* translocation, where the polymer is pulled by one of its ends. In the first case, the force can be applied via the introduction of an electric field accompanied by a charge gradient [10,29–32], or as the effect of a molecular machine capable of producing movement in the pore [16,24,25]. In the second the pore takes a more passive stand. This end-pulled force [33–36] emulates the action of experimental setups like AFM [37], optical or magnetic tweezers [38].

While the so-called *active-pore* and *end-pulled* translocation are the primary focus of this review, it is important to note that these are only two of the many other possible mechanisms that can facilitate the passage of a polymer through a membrane. For instance, chaperone-like elements can facilitate translocation by binding to the chain on the *trans*-side of the pore, thus preventing backsliding into the *cis*-region. [39,40], while active matter-driven approaches leverage the self-propelling properties of active particles of different shapes to exert an effective force on the polymer chain [41–43], driving the translocation forwards.

All these systems have been studied considering both computational and experimental approaches, so that analytical developments regarding multiple topics such as scaling behavior [22,44–46], free energy calculation [8,47,48], or force propagation [49–51] have become quite relevant.

In this review, we will focus on the different time-dependent active translocation. We will consider a particular coarse-grained polymer model, reviewing both results and behaviors of the chain under different drivings, pore geometry and site force applications. Section 2 will introduce the polymer model and its units. Sections 3 & 4 will focus on the different models of active pores and end-pulled systems, respectively.

In Section 5 we will introduce, as a specific application of polymer translocation, some new results concerning the analysis of the simulated trajectories of realistic protein chains, with the objective to infer the determination/sequencing of their secondary structure. Section 6 ends the paper with some conclusions and the opening to future applications.

2. Polymer model

The model used through this review describes a three-dimensional chain formed by N identical monomers. Bonds are described by harmonic interactions, and all beads are subjected to bending and excluded volume potentials. The harmonic bond term is given by

$$V_{\mathrm{el}}(d_i) = \frac{k_{\mathrm{el}}}{2}\sum_{i=1}^{N}(d_i - d_0)^2, \tag{1}$$

where k_{el} is the elastic constant, $d_i = |\mathbf{r}_{i+1} - \mathbf{r}_i|$ the distance between consecutive beads, with $\mathbf{r}_i$ being the position vector of the ith monomer, and d_0 the equilibrium distance between them. The bending energy of the chain is described by

$$V_{\mathrm{b}}(\theta_i) = -k_{\mathrm{b}}\sum_{i=1}^{N}\cos(\theta_i - \theta_0), \tag{2}$$

where k_{b} is the bending constant, θ_i the angle formed by three consecutive monomers $i-1$, i, and $i+1$ of the chain, and θ_0 is the equilibrium angle, taken as $\theta_0 = 0$ in this model.

Lastly, the steric repulsion between beads and between the beads and the pore is given by a truncated Lennard-Jones potential

$$V_{\mathrm{LJ}} = 4\epsilon\sum_{i\neq j=1}^{N}\left[\left(\frac{\sigma}{r_{ij}}\right)^{12} - \left(\frac{\sigma}{r_{ij}}\right)^{6}\right] + \epsilon, \tag{3}$$

This potential only applies when the distance between either monomers i and j or a monomer i and the pore, denoted by r_{ij}, is less than or equal to $2^{1/6}\sigma$. For larger distances, the interaction is assumed to be zero, since no steric interactions can occur.

The system is integrated considering overdamped Langevin dynamics, with the equations of motion in three dimensions resulting in

$$m\gamma\dot{\mathbf{r}}_i = -\nabla_i V_{\mathrm{el}}(d_i) - \nabla_i V_{\mathrm{b}}(\theta_i) - \nabla_i V_{\mathrm{LJ}} + \mathbf{F}_{\mathrm{drv}}(t) + \mathbf{F}_{\mathrm{wall}} + \sqrt{2m\gamma k_B T}\xi_i(t), \tag{4}$$

where m and γ are the mass and damping of each monomer respectively, and $\xi_i(t)$ represents the white noise associated with thermal fluctuations, considered as both white and gaussian, such that

$$\langle\xi_{i,\alpha}(t)\rangle = 0 \quad ; \quad \langle\xi_{i,\alpha}(t)\xi_{j,\beta}(t')\rangle = \delta_{i,j}\delta_{\alpha,\beta}\delta_{t,t'}$$

with $i = 1, \ldots, N$ and $\alpha, \beta = x, y, z$.

The steric interaction is separated in two terms, one for interactions between beads (V_{LJ}) and another for the interactions with the pore, namely F_{wall}. The second term, $\mathbf{F}_{\mathrm{drv}}(t)$, is the force driving the translocation, and will vary both in application and expression through this work. Fig. 1 shows the driving force for both the pore-driven ($F_{PD}(t)$) and end-pulled ($F_{EP}(t)$) cases, showing their corresponding application site.

2.1. Parameters and units of the model

Multiple parameters of the model are fixed beforehand: the bond equilibrium distance was taken as $d_0 = 1$, with the elastic constant $k_{\mathrm{el}} = 1600\epsilon/d_0^2$ to ensure non-extending chain behavior. Temperature was set to $k_{\mathrm{B}}T = 0.1\epsilon$, and the Lennard-Jones potential parameters are $\epsilon = 0.3$ and $\sigma = 0.8d_0$.

The dimensions of the pore are $\mathrm{L_M} = 5.5\mathrm{d_0}$ and $\mathrm{L_H} = 2\mathrm{d_0}$, and is modeled with the same excluded volume parameters as the Lennard-Jones potential between beads. These dimensions allow for up to 6 monomers to fit inside the pore at all times, in a straight line.

To rescale the model results to real values, the units of energy, length and mass have to be chosen. We took ϵ, d_0 and m as these units, thus resulting in a Lennard-Jones timescale of $t_{\mathrm{LJ}} = (md_0^2/\epsilon)^{(1/2)}$, which, after adjustment to our overdamped regime, corresponds to $t_\gamma = \gamma t_{\mathrm{LJ}}^2$.

To establish a relation of our units to real magnitudes we can compare it to a DNA chain at room temperature, thus fixing $k_{\mathrm{B}}T = 4.1$ pN nm. Since $k_{\mathrm{B}}T = 0.1\epsilon$ in our program, the energy unit $\epsilon_0 = 41$ pN nm. Additionally, we can set $d_0 = 1.875$ nm and $m = 936$ amu [52]. This way, we already obtain the units of time as $t_{\mathrm{LJ}} = 0.38$ ps, and the unit of force as $\epsilon/d_0 = 21.9$ pN.

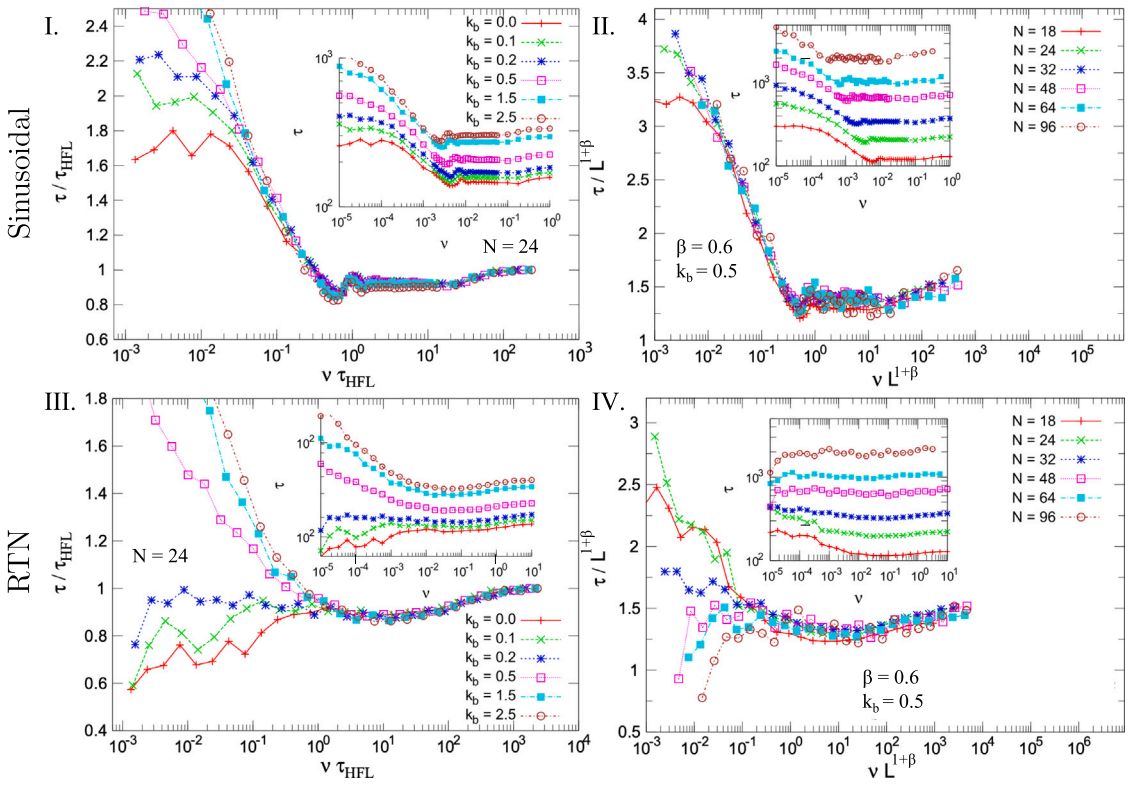

Fig. 2. Translocation curves for polymers under active pore drivings. **I.** Translocation times versus frequency for chains of length $N = 24$ and different bending constants k_b under sinusoidal driving. Axes are rescaled by the TT at high frequency. Inset shows the raw curves. **II.** Translocation times versus driving frequency for chains with the same bending constant and different length N, rescaled with Eq. (8), under sinusoidal driving. Inset shows the raw curves. **III.** Translocation times versus frequency for chains of length $N = 24$ and different bending constants k_b under RTN driving. Axes are rescaled by the TT at high frequency. Inset, raw curves. **IV.** Translocation times versus driving frequency for chains with the same bending constant and different length N, under RTN driving. Axes are rescaled by Eq. (8). Inset shows the raw curves.

3. Active pores

Active pores are characterized by their ability to modulate the translocation of polymers via mechanisms intrinsic to the pore structure or its immediate surroundings. Interest in the field of polymer translocation started with the experimental findings of Kasianowicz et al. [1], which used a lipid bilayer with α-hemolysin pores in conjunction with a voltage bias to characterize individual nucleotides of a chain by their respective channel blockage, eventually resulting in the creation of a series of nanotechnological devices for biosensing [5,6] and sequencing. Of particular interest is the device offered by Oxford Nanopore Technologies, a nowadays commonly used instrument fundamental in DNA sequencing [15].

Regarding the dynamics, the mechanisms driving the translocation can involve multiple phenomena, such as changes in the pore's shape, the presence of motor proteins that pull or push polymers through the pore, or localized fields and gradients that exert force on the fraction of the translocating polymer within the pore. Active pore mechanisms often offer a more controlled and localized approach to driving polymer movement, leading to unique translocation dynamics according to the specific time dependence of the driving.

This section explores various time-dependent forces used to describe active pores in translocation mechanisms in different studies. Within the context of our model, two main driving forces have been explored: a sinusoidal interaction, characterized by its frequency (ν) and initial phase (φ), and a *Random Telegraph Noise* (RTN), where the force switches between 0 and a given maximum (or viceversa) at a characteristic timescale, named T. The explicit form of this forces can be found in Eqs. (5) & (6), respectively:

$$\text{Sinusoidal:} \quad F(t) = F_0[1 - \cos(2\pi\nu t + \varphi)] \tag{5}$$

$$\text{RTN:} \begin{cases} \langle F(t)\rangle = F_0 \\ \langle F(t)F(t')\rangle = 4F_0^2(1 + e^{-2(t-t')/T}) \end{cases} \tag{6}$$

where $F_0 = 0.3$ is the amplitude of the force and $\nu = 2\pi/T$ the frequency of the oscillation.

The main magnitude investigated in our simulations is the average translocation time (or TT), *i.e.* the average time needed for a given chain to cross the pore from the *cis*-side into the *trans* region. In particular, the studies focused on the dependence of that observable with the frequency of the driving ν, the length of the chain N and the rigidity of the polymer, encoded in the bending parameter k_b. All the information regarding the results from these drivings is summarized in Fig. 2 here below commented in detail.

3.1. Translocation times and frequency of the driving

The average translocation times (TTs) normalized by their high frequency values (τ_{HFV}) are shown in Fig. 2I & II for the sinusoidal and RTN drivings respectively as a function of the normalized frequency of the force ($\nu \cdot \tau_{HFV}$). The different curves correspond to chains of different bending parameter k_b that maintain the overall behavior unchanged. The non-normalized curves are reported in the top right inset of each figure.

In general, we can distinguish three clear regimes based on the frequency of the driving: one at low frequencies, characterized by a general high value of the translocation times (except for two of the chains in the RTN case, discussed later), a moderate value in the opposite range at high frequencies, where the TTs tend to saturate, and an intermediate frequency region, which possesses a global minimum of the translocation times.

High frequency regime. At high frequencies, the force changes much faster than the typical timescale of polymer motion. Thus, the chain

feels an effective force corresponding to the time average of the driving, F_0, the same in both the sinusoidal and RTN cases, where the high frequency TTs for both drivings tend to coincide.

Low frequency regime. Conversely, in the low frequency regime the translocation is determined by the initial phase of the force. In this region the typical translocation time is much smaller than the period of the driving, therefore the force remains practically constant throughout the translocation, only governed by its initial state, encoded in the phase ϕ.

Situations in which the force starts at low values (or 0 in the case of the RTN) lead to slow translocation, thus significantly increasing the average TTs, as observed in the results. The low values observed in some of curves of the RTN case (see panel III of Fig. 2) at low frequency values correspond to the circumstances in which the chains with driving close to 0 in their initial state exit the pore on the *cis*-side, and are eliminated from the ensemble averages. In this case, only due to simulation bias, the statistics only includes the most favorable translocation with lower TTs and for these reason the curves show low TT values. This effect is more relevant for low bending values.

Intermediate frequencies. Between the two regions defined before, a third one can be observed, characterized in both drivings by the presence of a global minimum in the TTs. In the sinusoidal regime, we observe a series of oscillations inside this region, whereas the RTN has a more parabolic character, with a large optimum TT region.

Regardless of the specific driving, the appearance of these minima shows the occurrence of the Resonant Activation effect [53–57], in which the characteristic passage time of a particular polymer chain synchronizes with the frequency of the force ν, thus leading to the appearance of a large minimum region. The Resonant Activation phenomenon is one of the many counterintuitive effects of the fluctuations in nonlinear systems, ubiquitous in all fields of science [58].

The existence of this minimum is especially robust in the sinusoidal driving, and its value has a linear relationship with its associated period, that holds true for whatever magnitude of the polymer, such as lengths or bending strengths. In particular, the minimum translocation time verifies the linear relation

$$T_{\min} = \alpha \langle \mathrm{TT} \rangle_{\min}, \tag{7}$$

where $T_{\min}$ is the period of the force associated with that particular minimum, and $\alpha \approx 1.36$ is a constant for the above described drivings. Taking the data for the sinusoidal driving of panels I & II of Fig. 2, the coefficient has been estimated for this review, resulting in $\alpha = 1.41 \pm 0.07$, compatible with 1.36. The coefficient was studied in other works, initially in 1D [19,23], and later in 3D [59], for chains of different characteristics and under different simulation conditions, changing the temperature and damping. A curve displaying this relationship can be found in Fig. 4, with the data taken from [18,19,59].

The Resonant Activation in polymer translocation has been also found by authors that have found optimal translocation times with different mechanisms. Cohen et al. [20] applied in 2D a constant translocation force, changing the width of the channel periodically. The same effect was observed, finding a critical frequency which lead to faster translocation. The synchronization took place between the frequency of channel changes and the typical translocation time of the polymer at the force used, resulting in TT curves very similar to the sinusoidal driving [19].

Ikonen et al. [52] analyzed simulations considering a 2D geometry as well. They found Resonant Activation in two different cases: one with a sinusoidal driving in absence of interactions with the pore (only steric repulsion), and another with a dichotomic random force and pore attraction. They derived a numerical expression that predicted the behavior caused by the sinusoidal driving seen in Fig. 2I & II, reproducing the oscillations around the minima, by taking into account that some initial phases are favored with respect to others: phases with low initial force can lead to either failed translocations, when the polymer exits the pore on the *cis*-side and therefore does not count in the average TTs, or longer translocations, which increase the average TTs.

3.2. Influence of polymer size

Fig. 2II & IV contain the translocation curves of polymers of different sizes with the same bending constant ($k_b = 0.5$) for the sinusoidal and RTN drivings, respectively. The raw curves without scaling are located in the top inset of each figure.

The curves follow a very similar trend, only changing the values of the TTs themselves: larger polymers take more time to cross the pore. Furthermore, the curves can be rescaled with the polymer size, according to the law

$$\langle TT \rangle_N \propto [(N-1)d_0]^{1+\beta} = L^{1+\beta}, \tag{8}$$

where $\beta = 0.6$ is the scaling exponent of the curves. This scale law is verified by the fact that all curves collapse on each other when applying it to both axes, eliminating the dependence on the polymer size. The decrease of τ for large polymers at low frequencies in the RTN case is due to the analogue effects of exit of the chains towards the *cis*-side equivalent to the low bending curves in panel III of the same figure. The relationship between polymer length and bending k_b is further explored in Section 3.3.

The exponent β of Eq. (8) can be connected to the parameters of the chain through the Flory exponent ν_F [60]. This magnitude depends on the rigidity of a polymer chain, and takes the value of $\nu_F = 0.5$ for the Freely Jointed Model (FJM, a polymer with only bonds between beads, completely flexible), whereas for a completely rigid rod $\nu_F = 1.0$ [61–63]. A Flory coefficient of $\nu_F = 0.6$ corresponds to chains with reduced rigidity and excluded-volume interactions between beads [62]. This is compatible with the chains of Fig. 2II & IV, since $k_b = 0.5$ is a low bending value in the context of our simulation.

Similar scaling laws have been found in other works. Furthermore, it has been shown that, depending on the size of the polymer chain and other parameters of the simulations, the scale law varies significantly. Studies on molecular machinery, using an ATP-based driving, showed that pore size matters in the scaling of the TTs [25]. A dependence of $\langle TT \rangle_N \propto N(N - N_{\mathrm{pore}})^{\nu_F}$ with N_{pore} being the length of the channel was revealed. When using polymers with $N \gg N_{\mathrm{pore}}$, Eq. (8) is recovered.

By studying 2D Monte Carlo simulations of a chain translocating under the effects of electric fields, Luo et al. [64] found the presence of two scaling laws with the chain size. They proposed the scaling $\langle TT \rangle_N \propto N^{2\nu_F}$ for small polymers, and the law $\langle TT \rangle_N \propto N^{1+\nu_F}$ for larger polymers, without any pore size effect.

These authors in a later publication [61] considered a 3D system very similar to the model in Section 2. When studying translocation dynamics at constant forces, they observed two different scale laws with polymer size N, called "slow" or "fast" dynamics. At low forces, or high damping coefficients, the polymer translocated in a slow manner and under equilibrium conditions, thus $\langle TT \rangle_N \propto N^{1+\nu_F}$. For fast translocations, the equilibrium assumption breaks down, leading to $\langle TT \rangle_N \propto N^{1.37}$.

These studies show the high variability of the scaling exponents with dimensionality, chain features and the medium in which the simulations take place. Palyulin et al. published a review [65] compiling estimations of these exponents introduced by other authors, associating the multitude of different reported scaling exponents with out of equilibrium translocation dynamics.

This variability in the scaling coefficients has motivated other authors to introduce additional terms in the formula, to include further effects. In particular, Sarabadani et al. [21,66] introduce a term of pore friction, with the aim to describe the polymer experiencing a drag effect due to the narrowing of the pore, that translates into a linear dependence of the translocation time with polymer size N. Applying a force of the form $F(t) = F_{\mathrm{const}} + A\sin(\omega t + \psi)$, they find:

$$\tau = \tau_{\mathrm{stat}} + \frac{1}{F_{\mathrm{const}}} \int_0^{\tau} A \sin(\omega t + \psi) dt \tag{9}$$

$$\tau_{\mathrm{stat}} = \frac{A}{(1+\nu_F)F_{\mathrm{const}}} N^{1+\nu_F} + \frac{\gamma_{\mathrm{pore}}}{F_{\mathrm{const}}} N, \tag{10}$$

where γ_{pore} is the pore friction, and τ_{stat} represents the average translocation time with the constant force F_{const} only.

Eq. (9) can be subjected to different approximations, depending on the frequency ω and the relationship between the amplitude of the oscillations A and F_{const}, and the authors claim a good agreement between theory and simulations in Refs. [21,66]. Independently of the force and frequency regimes, Eq. (9) introduces a linear dependence of the translocation time scaling with the polymer length N, relevant for small chains. At large N, the simpler scaling law $\langle TT\rangle_N \propto N^{1+\nu_F}$ is recovered.

An attempt to fit the data presented in Fig. 2 with Eq. (9) has been performed, obtaining a collapse of the curves similar to the one shown, so not revealing a significant improvement with respect to Eq. (8). In this sense, we are not able to confirm the need of the inclusion of an additional porous friction term.

3.3. Effect of the bending constant (k_b)

Fig. 2I & III contain the mean translocation time curves for chains of equal length ($N = 24$) at different k_bs, ranging from 0.0 to 2.5 in model units. The top inset shows the curves without the scaling applied, clearly depicting the dependence of the TTs with k_b.

For both sinusoidal and RTN drivings, higher chain rigidity leads to higher translocation times. This can be explained by the conformation adopted by the polymer with the bending constant: when the translocation begins, the position of the monomers on the *cis*-side assembles into an elongated conformation for high rigidity, whereas lower bending values tend to have monomers closer to the entrance, facilitating translocation. As a consequence, the frequency of the minimum TT also changes with k_b.

The case of low TTs observable at low frequency in Fig. 2, panels III and IV for low bending values and long chain respectively, can be understood by considering the motility of the chain that, in those conditions, lead to an higher probability of interacting with the membrane wall. This circumstance is at the origin of the escape of the chain from the pore to the *cis*-side when the initial driving is zero, thus reducing the statistics of the trajectories which would increase the average TT, as already commented in Section 3.2.

4. End-pulled approaches

In end-pulled translocation, the pore takes a passive role in the process, with the driving being applied to one of the extremes of the polymer chain. This setup, as stated before, is meant to reproduce the experimental conditions in Atomic Force Microscopy (AFM) [37], optical and magnetic tweezers [23,38].

The most common end-pulling approaches are performed in two main categories: *force bias* and *constant velocity*. In the first, a cantilever pulls the polymer's end by applying a force, while in the second an harmonic spring is used to pull the polymer at a constant speed.

This method is particularly useful for exploring non-equilibrium effects, such as chain stretching, tension propagation, and pore–particle interactions [67,68]. While the driving at constant force emphasizes the polymer's mechanical response and deformation in the dynamics, the pulling at constant velocity allows to highlight the role of potential energy barriers and their relationship with entropic configurations [36].

The two categories are thus somehow complementary, and we will explore each of them separately in the following subsections.

4.1. Force biased pulling

We studied the effects of applying a time-dependent force onto the end of our polymer to drive the translocation [59]. Differently than the driving applied on the polymer by the pore, where the force direction maintains along the pore axis, in the end-pulled case the force can be applied in two different modes in the *trans*-side of the membrane: the *longitudinal*, applied in the direction of the pore's length, and the *transversal* perpendicular to it. Both share the time dependence:

$$F(t) = F_{\text{const}}\hat{x} + F_0 \cos(2\pi\nu t + \varphi)\hat{r}, \tag{11}$$

where F_{const} is a constant term added to facilitate translocation, assigned either 1.8 or 0.3 in program units for longitudinal and transversal driving respectively, $F_0 = 1.5$ is the amplitude of the variable term, ν is the frequency and φ the random initial phase. The unitary vector $\hat{r}$ takes the value of $\hat{x}$ for the longitudinal force and $\hat{y}$ for the transversal one.

In the following, we compare the results of both TTs and length scale obtained in end-pulled translocation with those obtained in pore-driven translocation.

4.1.1. Translocation times

The outcomes of a frequency sweep of the average translocation times for both longitudinal and transversal drivings have been reported in Fig. 3(i) & (iii), respectively, for chains of equal length $N = 30$ and different bending constants k_b. The *longitudinal* pulling reveals identical behavior to those found in Fig. 2I. This result can be expected, since only the point of application of the force has changed, not the driving. Conversely, the *transversal* pulling presents a different TT behavior as a function of the frequency, with high TTs at high frequencies and low values at low frequencies. In the following, we comment the three frequency regimes separately, and discuss the differences between the pulling modes, *longitudinal* and *transversal*.

For both modes, at high frequencies, the force experienced by the polymer is an average over time of the driving, because the polymer dynamics' timescale is much longer than the force period. Thus, only the constant term F_{const} of the force contributes to the polymer movement. Furthermore, the horizontal lines on the right hand-side of each curve of Fig. 3(i) & (iii) correspond to the TT values calculated with constant forces only, thus proving this hypothesis. The value of the TTs at high frequency result very different for longitudinal and transversal drivings. This gap is due to the different constant forces F_{const}, 1.8 and 0.3 for the longitudinal and transversal respectively. Equal F_{const} would provide identical high frequency limits in the two cases.

In the low frequency (LF) section we can notice a real qualitative difference in the behavior between the two modes: TTs values are much higher at LF than at high-frequency (HF) for the longitudinal case, and viceversa in the transversal case. The reason for this divergent behavior lies in the fact that in the limit of low frequencies, the force is completely determined by its initial phase, which maintains its value during all the dynamics.

Because of the above, the discrepancy between the two modes can be understood in connection with the different directions of the applied force. In fact, while in the longitudinal case some phases induce negative initial values of the force, so slowing down the translocation, the same phases in the transversal driving, where the force is applied perpendicularly to the pore axis, result in an identical contribution as the opposite phases give equal outcomes. This way a positive push (due to the walls reaction) applies independently of the sign of the force. Particularly, all initial phases (save for $\varphi = \pi/2$ or $3\pi/2$, which give 0 force) contribute positively to the translocation in the transversal case, thus obtaining smaller TTs with respect to its high frequency limit.

The mid frequency regime exhibits the global minima in the TTs expected from the Resonant Activation phenomena in both drivings, caused by the synchronization of the mean TTs and the period of the force. The region around the minima of both modes exhibit a trace of an oscillating behavior characteristic of the sinusoidal force [18], which is very similar between the longitudinal case (Fig. 4, panels (i) & (ii)) and the corresponding pore-driven results (Fig. 2, panels I. and II.)

The linear relationship between the minimum of Eq. (7) and its associated period holds for the end-pulled setup, but with different coefficients for each mode. The longitudinal force maintains the $\alpha_{\text{Ep, long}} \approx 1.36$ previously observed for the RTN driving, shown in Fig. 4, whereas

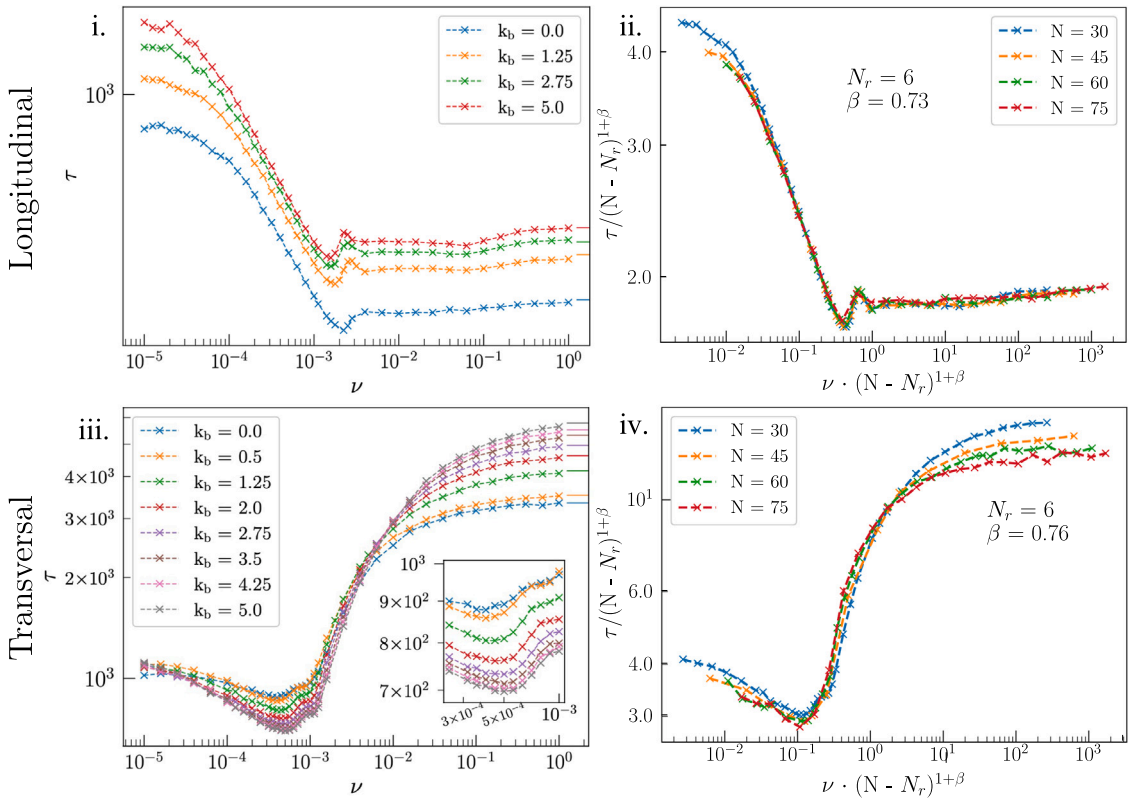

Fig. 3. Translocation curves for polymers under end-pulled drivings. **(i).** Translocation times versus frequency for chains of length $N = 30$ and different bending constants k_b (values shown in the legend) under longitudinal driving. **(ii).** Translocation curves of chains of identical bending constant ($k_b = 1.25$) and different lengths (values shown in legend) under longitudinal driving. Both axes are rescaled according to Eq. (12), with the fitting parameters shown in the image. **(iii).** Translocation times versus frequency for chains of length $N = 30$ and different bending constants k_b (values shown in the legend) under transversal driving. Inset corresponds to a zoomed plot near the minima. The horizontal lines on the right edges of both plots correspond to simulations done at constant force equal to the temporal average of the driving. **(iv).** Translocation curves of chains of identical bending constant ($k_b = 0.5$) and different lengths (values shown in legend) under transversal driving. Both axes are rescaled according to Eq. (12), with the fitting parameters shown in the image.

the transversal direction of the force leads to a higher coefficient $\alpha_{\text{Ep, trans}} = 2.9$. The values are approximately twice each other, explained by the positive contribution that opposite phases have in the transversal case. Fig. 4 shows the relationship between the minimum translocation time and the corresponding force period for chains of different characteristics under the different sinusoidal drivings and modes.

4.1.2. Dependence on polymer length N

Fig. 3(ii) & (iv) show the mean translocation time as a function of the frequency for different bending constant k_b and different polymer size N, where both axes are scaled according to the scaling similar to the one presented in Ref. [25] which essentially accounts for the number of monomers N_p inside the pore – 5 in average – plus 1:

$$\langle TT \rangle_N \propto (N - N_r)^{1+\beta}, \tag{12}$$

where $N_r = N_p + 1 = 6$ and β is the scaling coefficient which also depends on the stiffness of the chains.

The inclusion of the number of monomers inside the pore on the scale law has been considered necessary to correct size restrictions imposed by the channel on the polymer. Nevertheless, the specific form in which N_p is considered, is different for specific scaling laws of different drivings.

The scaling coefficient β has been related to the Flory coefficient ν_F, as commented in Section 3. A fit to chains of sizes $N = 30, 45, 60, 75$ was made for each value of the bending coefficient k_b, showing a monotonic increase of β with k_b, as shown in Table 1. The values are well within the range of the Flory coefficient for a chain with excluded volume interactions and the rigid rod ($\nu_F \in [0.6, 1.0]$).

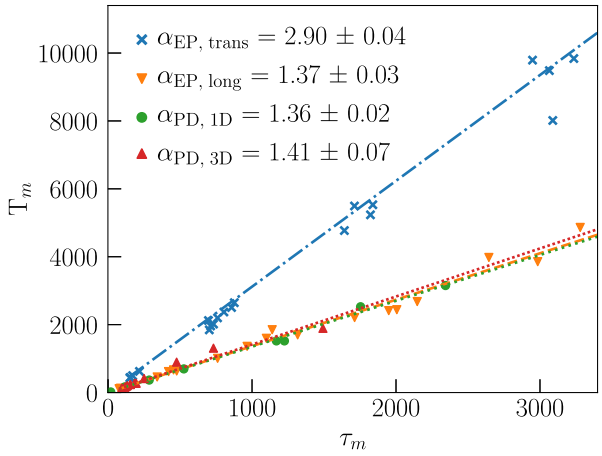

Fig. 4. Relationship between the minimum average translocation time (τ_m, x-axis) and its associated period (T_m, y-axis) for chains of different lengths, bending constants, in the case of sinusoidal drivings. In blue crosses and orange inverse triangles the end pulled transversal (EP, trans) and longitudinal (EP, long) modes from Fig. 3. In green circles the data points of the pore-driven in 1D driving (PD, 1D) of [19]. In red triangles, points for the pore-driven in 3D (PD, 3D) from ref [18]. All points are shown with their corresponding fitting line, whose coefficients are reported in the label.

Huopaniemi et al. [69] studied the end-pulled translocation of chains under different constant forces in 2D, finding two different regimes for the scaling with polymer size depending on the magnitude

Table 1
Exponent for the scaling of the translocation times as a function of the number of monomers N for chains of different bending constants, according to Eq. (12) $\langle TT\rangle_{\rm N} \propto (N-6)^{1+\beta}$. The uncertainty in the determination of the exponents was on the order of 0.03 for the longitudinal mode, and 0.10 for the transversal.

$k_{\rm b}(\epsilon)$	0.0	1.25	2.75	5.0
$\beta_{\rm EP,long}$	0.64	0.73	0.79	0.83
$\beta_{\rm EP,trans}$	0.59	0.76	0.82	0.92

Table 2
Exponents for the evolution of the translocation time under pore-driven dichotomous forces as a function of N for chains of different bending constants, with $\langle TT\rangle_{\rm N} \propto N(N-6)^{\beta}$.

$k_{\rm b}(\epsilon)$	0.0	0.5	1.5	2.5
β	0.47	0.50	0.65	0.73

of the force: $\langle TT\rangle_{\rm N} \propto N^{1+2\nu_{\rm F}}$ for weak forces, and $\propto N^2$ for strong and moderate forces.

In later works, Sarabadani et al. [33,70] expanded on the idea under the so-called Iso-Flux Tension Propagation theory to deeper investigate the relationship of the TTs with the polymer size. They found an additional N^2 that corresponds to be the asymptotic high force limit of the scaling, influenced by non-equilibrium phenomena and interactions with the pore on the *cis*-side of the membrane, and derived an analytical expressions for the passage times.

Menais [49] also studied the scaling exponents of end-pulled translocation at constant force, finding at a particular force value a TTs dependence $\propto (N-4)^{1.85}$. The correction applied to polymer size was due to the "retracting tail" effect, where the last monomers of a chain undergo translocation much faster than the rest at moderate forces, the polymer thus exhibiting an effective size smaller than N.

For a comparison, in Table 2 we collect the scaling values obtained in Ref. [25], where the pore driving force was provided by a dichotomous motor fueled by ATP. The scaling there found in the simulations follows the shape $\tau \propto N(N-6)^{\beta}$, slightly different from those up to now discussed. However, those exponents follow again a monotonic increase as a function of the chain stiffness, and are surprisingly identical with the scaling exponent valid for the gyration radius at different length, also there obtained [25].

Dependence on bending coefficient $k_{\rm b}$

In this section we will focus on the study of the dependence of the translocation times with the bending constant k_b, as shown in Fig. 3i. & iii.

For the longitudinal mode, the results are essentially equivalent to those of active pore with the same sinusoidal driving: higher rigidity leads to higher mean translocation times, due to the conformations the stiffer chains adopt during the process, with the center of mass further from the pore entrance thus taking longer to traverse the pore.

On the transversal mode, however, the dependence with the frequency, in general, does not follow the same qualitative behavior as the longitudinal one.

In fact, while at high frequencies, when an effective constant force is applied on average, high bending values present larger mean TTs than those of lower k_b, in a similar way as in the longitudinal case. Meanwhile, in the middle frequency range, around $\nu = 10^{-2}$, the relationship inverts; stiffer chains translocate faster. This effect is associated to the interactions with the walls on the *trans*-side of the pore. The reaction forces are larger – and the impact of the polymer with the membrane walls is more frequent – for stiffer chains, thus providing an additional forward-directed effective force.

Finally, the behavior at low frequencies appears to saturate for all curves, regardless of $k_{\rm b}$.

To confirm the hypothesis that stiffer chains cause the wall to react with higher forces, we performed additional simulations in which chains of varying lengths and bending constants were pulled with a constant force, mimicking the maximum transversal force in the sinusoidal driving.

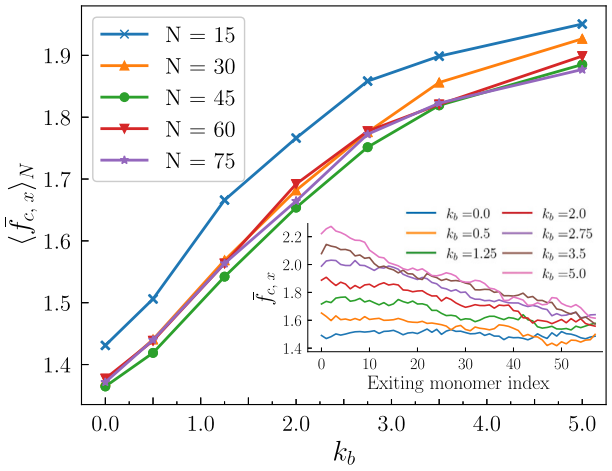

Fig. 5. Mean reaction force of particles colliding with the walls of the *trans*-side of the pore averaged over all monomers and multiple simulations $\langle \bar{f}_{c,x} \rangle$ as a function of the bending constant k_b for chains of different lengths, shown in the legend. In the inset, the average force felt by each monomer $\bar{f}_{c,x}$ as a function of their exit order for chains of $N = 75$.

In these simulations we calculated the mean reaction force over time $\bar{f}_{c,x}$ a particle experiments when colliding with the walls in the *trans*-side, averaged over all the monomers ($\langle \bar{f}_{c,x} \rangle_N$). The results are shown in Fig. 5. From the figure, it is evident that chains with higher bending constants experience greater reaction forces, with a saturation trend at high persistence lengths $l_{\rm p}$ (with $l_{\rm p} = k_b d_0 / k_{\rm B}T \approx 10 k_b$), *i.e.* high bendings, where all the chains are approximately rigid. Short chains $N < 30$ present higher forces than longer ones (see $N = 15$ in the figure). This effect is due to fact that the bending does affect the force felt by the different monomers in the translocation according to the order in which they exit from the pore. In fact, the inset of Fig. 5 shows $\bar{f}_{c,x}$ with the index of the monomer in exit order, where we see a clear decreasing trend of the force, steeper for higher values of the bending. Short chains do not have the time to experience reduced forces in the kinetics.

4.2. Constant velocity pulling

As stated before, velocity pulling applies a constant speed to the first monomer of the polymer chain, mimicking experimental setups based on AFM, optical and magnetic tweezers [23,37,38].

Many authors [8,71,72] have studied the free energy functions and surfaces associated to polymer translocation. There is a certain degree of consensus regarding the dynamics of the polymer: the change in conformational entropy induced by the restrictions imposed to the polymer while inside the pore, as well as between the sides of the membrane if the environment changes significantly (for example, changes in chemical potential, pressure or temperature), imposes an effective energy barrier to be passed during the translocation. This free energy function has been deduced [8], for a polymer of length N crossing a non-extended pore, as

$$\frac{F_{N_{\rm trans}}}{k_{\rm B}T} = (1-\gamma_2)\ln(N_{\rm trans}) + \\ + (1-\gamma_1)\ln(N - N_{\rm trans}) - N_{\rm trans}\frac{\Delta\mu}{k_{\rm B}T}, \tag{13}$$

where $N_{\rm trans}$ is the number of monomers in the *trans*-side of the membrane. The first two terms represent the conformational entropy of the chain on the *trans* and *cis* sides of the membrane, respectively, and

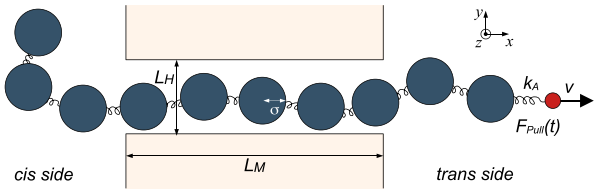

Fig. 6. Scheme of the force spectroscopy simulation setup, illustrating the polymer chain in violet color. The red dot represents the connection to the cantilever, pulled away at a constant velocity v, and k_A is the elastic constant of the spring through which the force is measured during the translocation.

the last term is associated to the change in chemical potential between the two regions $\Delta\mu$. The parameters γ_1 and γ_2 correspond to scaling exponents associated to the polymer's partition function in each region, and depend on the particular membrane geometry and environment on each side, according to [8,71].

This function leads to a symmetric, smooth barrier for the typical case in translocation experiments, with $\gamma_1 = \gamma_2$ and $\Delta\mu = 0$. Introducing a pulling force or velocity into the system leads to a shift in this energy barrier.

In Ref. [71], through the use of the Jarzynski equality, $\langle e^{-W/k_BT}\rangle = e^{-F/k_BT}$ – which allows for the estimation of free energy potentials from nonequilibrium measurements – the authors perform Langevin simulations pulling at constant speeds, revealing a similar free energy potential as Eq. (13), but with a much sharper barrier. They associated this effect with the inclusion of vibrational degrees of freedom introduced in the model with respect to the original theory [8], finally proposing the new expression

$$\frac{\Delta F_{N_{\text{trans}}}}{k_BT} \propto \left[(N - N_{\text{trans}})^{\alpha} - \left(\frac{N}{2}\right)^2\right], \tag{14}$$

with an explicit scaling behavior with the polymer length according to a power law with exponent $\alpha = 1.53$. The authors demonstrated the validity of their findings by taking the energy barrier data calculated in Ref. [72], applying Eq. (14), and collapsing the curves at different N into a single curve.

From the study of the free energy functions associated to the translocation dynamics, the model presented in Section 2 has been also used to investigate the possibility to describe the translocation process as a single barrier crossing event [36,56,73,74]. In fact, the possibility to describe the translocation process under a unique potential barrier for all the monomers of the polymer is not an obvious modelization. The problem is that the individual monomers need to overcome a different entropic barrier generated by the branch of the chain outside the pore (see Eq. (13) and Ref. [36])

Following force spectroscopy setups, one of the edges of a polymer chain with N monomers and k_b bending constant has been attached to a harmonic cantilever with elastic constant k_A, moving at a constant speed v, resulting in a loading rate $r = k_A v$. A scheme of this setup is presented in Fig. 6.

Fig. 7 shows a typical trajectory of a short chain of $N = 32$ and very small bending constant, revealing two distinct regimes: The first corresponds to the exponential increase of pulling force as the polymer enters the pore, which begins to exponentially decrease when the *trans*-side is reached by the first monomer, where the reactions against the *trans*-wall start facilitating the translocation event. In fact, the exponential decrease starts when the 7th monomer enters the pore, independently of the chain size N, due to the constraint that the extended pore is ≈6 monomers long. These observations reinforced the evidence that the energy barrier of the translocation is mainly associated with the reactions between the polymer and the walls themselves.

The maximum value of the force in the trajectory has been averaged over multiple experiments and different pulling velocities. The resulting curve has been fitted through the use of the Friddle–Noy–DeYoreo

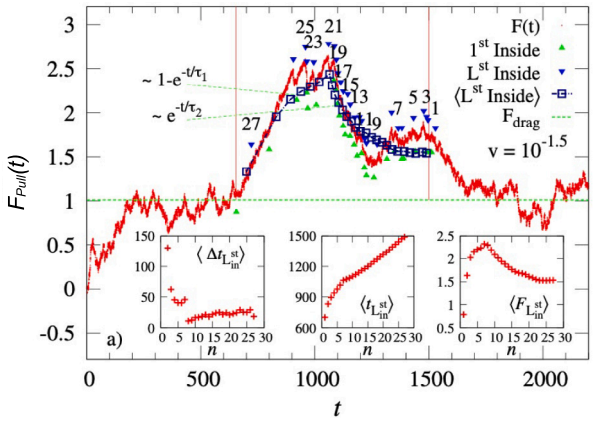

Fig. 7. Pulling measurements of force as a function of time $F_{\text{pull}}(t)$ for a chain of $N = 32$ monomers pulled at $v = 10^{-1.5}$ and with $k_b = 10^{-3}$. The small arrows above and below the curve indicate, respectively, the time of entrance and exit of each monomer, labeled near the arrow. The square symbols indicate the average value of the force at the entrance events.

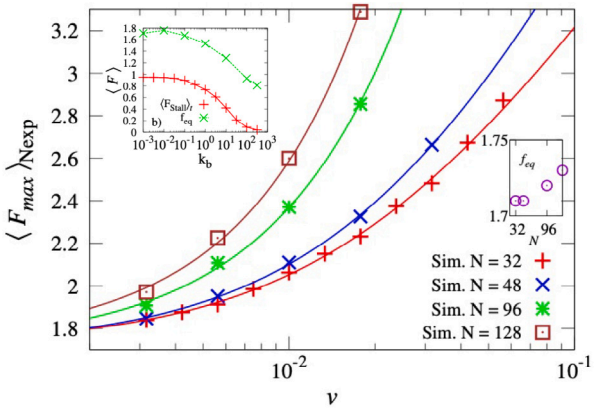

Fig. 8. Values of maximum average force $\langle F_{\text{max}}\rangle$ measured for chains of different lengths (shown in legend) as a function of the pulling speed v. The continuous lines correspond to the fitting curves from Eq. (15). Top left inset shows the dependence of the minimum translocation force (f_{eq}) with the bending constant, and the comparison with the stalling force (more details on the original paper [36]). Right inset, dependence of the minimum force f_{eq} with the length of the chain N.

(FND) [75] theory. This model was developed to interpret the force spectra observed in single-molecule force spectroscopy experiments and takes into account possible back and forth movements of the chain, allowing for the study of slow pulling velocities. The prediction made by this model is contained in the following equation:

$$\langle F_u\rangle = f_{\text{eq}} + \frac{k_BT}{x_u} e^{\left(\frac{k_u(f_{\text{eq}})k_BT}{rx_u}\right)} E_1\left(\frac{k_u(f_{\text{eq}})k_BT}{rx_u}\right) \tag{15}$$

with $\gamma \approx 0.577$ is Euler's constant, x_u the effective position of the barrier, $E_1(z) = \int_z^\infty \frac{e^{-s}}{s} ds$ is the exponential integral and f_{eq} the necessary force to equilibrate the refolding rates in the model (minimum force for translocation in the system), which can be related to the energy difference between states as $f_{\text{eq}} = \sqrt{2k_AG^+}$.

The results of the simulations and the corresponding fits are shown in Fig. 8, with the resulting fit parameters listed in Table 3 for chains of different lengths N. The agreement of the fits with the data appears clear, and induces to interpret G^+ as the energy difference between the *cis* and *trans* sides of the wall measured in the translocation. This interpretation is not obvious given the geometry of the system and requires a deeper investigation. G^+ is situated at $x_u \approx 0$, which corresponds to the pore entrance on the *cis* side in our model, and

Table 3
Parameters obtained from the fit of the maximum forces of chains of different sizes $N = 32, 48, 96, 128$ translocating at different speed with Eq. (15).

N	32	48	96	128	Error
x_u	0.11	0.08	0.0047	−0.008	≈80%
k_o	0.0027	0.0024	0.0017	0.0013	≈7%
f_{eq}	1.71	1.71	1.72	1.73	≈2%
G^+	7.34	7.34	7.35	7.36	

the minimum force necessary for the translocation seems to be weakly correlated to polymer size (see the right inset of Fig. 8), and strongly dependent on the rigidity of the chain, with stiffer chains requiring less force to translocate, on average (left inset of Fig. 8).

5. Protein translocation

The knowledge of the secondary structure of proteins is a fundamental aspect of molecular biology, constituting the basic framework of a protein's spatial conformation and functionality. The arrangement of alpha helices (α-helices), beta sheets (β-sheets), and random coils has a significant influence on the protein's stability, interaction with other molecules, and overall biological activity. Understanding secondary structure is essential for its insights into protein function, interactions, and the mechanisms underlying various diseases.

Traditional methods for determining protein secondary structure, such as Circular Dichroism (CD) spectroscopy, Fourier Transform Infrared (FTIR) spectroscopy, Nuclear Magnetic Resonance (NMR) spectroscopy, and X-ray crystallography have unique strengths and limitations. CD [76] and FTIR [77] provide rapid assessments of secondary structure content but with limited resolution. NMR spectroscopy delivers detailed structural insights, particularly for small to medium-sized proteins in solution, but is less effective for larger proteins and complexes [78]. X-ray crystallography offers high-resolution structural data but requires the challenging step of protein crystallization, capturing only static conformations [79,80]. Recently, cryo-electron microscopy (cryo-EM) has emerged as a powerful tool for visualizing large macromolecular complexes without the need to crystallize the molecules, yet it requires sophisticated equipment and expertise [81].

Similar approaches to those used in translocation-based DNA sequencing cannot be directly applied to proteins without significant modifications [82]. Proteins are composed of up to 20 different amino acids, making current-based characterization more complex. Additionally, the diversity of charge densities of these amino acids impede the effective use of the electric field approaches commonly employed for DNA, RNA, and other polymers [83,84], making the very translocation difficult. Various attempts using solid-state devices [85,86] or repurposed biological machinery [87,88] have been made, although these methods often result in fast, uneven movements of the molecule that limit both the resolution and the throughput of these experiments [89,90].

In this section we present preliminary results based on an application of end-pulled translocation to investigate the secondary structure of proteins. Using coarse grained models of these objects, introduced in previous works [91–97], we simulate and study the behavior of the native structure of a known protein composed of α-helices. A more complete study with inclusion of β-sheets and mixes of both will be delivered elsewhere. Coarse-grained models simplify the representation of proteins by grouping atoms into larger units, so reducing the computational complexity while preserving the essential structural and dynamic properties [98–100]. The chosen coarse-grained model has been carefully parametrized to reflect key physical characteristics, ensuring that it accurately reproduces the native conformations and secondary structure elements of these proteins [94,95].

The model describes the proteins as a folded one-dimensional chain formed by a series of monomers joint together by elastic springs, that also interact through bending elasticity, Van der Walls and dihedral potentials, in order to correctly recover a typical native three-dimensional structure. Each of those beads represents an individual amino acid and, depending on both the sequence of the protein and the secondary structure element they belong to, present adequate Van der Walls and dihedral coefficients.

Following Refs. [94,95], the harmonic potential associated to the elastic interaction is given by

$$V_{\mathrm{el}}(d_i) = \frac{k_{\mathrm{el}}}{2}\sum_{i=1}^{N}(d_i - d_0)^2, \tag{16}$$

where $k_{\mathrm{el}} = 1000\epsilon/d_0^2$ is the elastic constant of the interaction, $\mathbf{r}_i$ the position vector of the ith monomer, $d_i = |\mathbf{r}_{i+1} - \mathbf{r}_i|$ the distance between consecutive beads and d_0 the equilibrium distance. The bending energy of the chain is described by

$$V_{\mathrm{b}}(\theta_i) = k_{\mathrm{b}}\sum_{i=1}^{N}(\theta_i - \theta_0)^2, \tag{17}$$

where $k_{\mathrm{b}} = 20\epsilon$ is the bending constant, θ_i represents the angle formed by the three adjacent monomers $i-1$, i, and $i+1$, and θ_0 is the equilibrium angle. In this particular model, the equilibrium angle is fixed at $\theta_0 = 105°$.

The main ingredient to achieve the folded conformation of the protein in the model is the presence of the Van der Waals interactions

$$V_{\mathrm{VdW}} = 4\epsilon\left(\frac{A}{r^{12}} - \frac{B}{r^6}\right), \tag{18}$$

where the parameters A and B for each monomer depend on the sequence of the protein, a. Each aminoacid is classified into three categories regarding their hydrophobic character: hydrophobic (H), polar (P) or neutral (N). Hydrophobic residues tend to stick together to avoid the solvent, and thus H–H interactions are attractive, with $A = 1.2d_0^{12}$, $B = 1.2d_0^6$. Interactions involving neutral and polar aminoacids (N–N, N–P, N–H, P–P and P–H) are described via a simple Lennard-Jones potential, only presenting a repulsive force accounting for their volume, with $A = 1.2d_0^{12}$, $B = 0$.

The final ingredient for the establishment of the secondary structure elements is the dihedral interaction. The dihedral angle ψ_i is the one formed by residues $i-1$, i, $i+1$ and $i+2$ allows the torsion of the bead chain, and, together with the Van der Walls contribution, forms to α-helices or β-sheets. The potential energy associated to the behavior of these angles is

$$V_{\mathrm{dih.}} = C(1-\cos(\psi_i)) + D(1-\cos(3\psi_i)) + \\ +E\left(1+\cos\left(\psi_i + \frac{\pi}{4}\right)\right), \tag{19}$$

where the coefficients C, D and E depend on the secondary structure element each angle belongs to. For α-helices, requiring a torsion of the dihedral angles to form its characteristic appearance, $C = D = E = 1.2\epsilon$. For the neutral regions connecting α-helices and β-sheets to each other, which we will name as γ-loops and with no discernible secondary elements, $C = E = 0$ and $D = 0.2\epsilon$.

The translocation pore used consists of a cylindrical cavity of radius R_{p} and length $L_{\mathrm{p}} = 10d_0$ carved within a solid wall constructed with a diamond lattice structure of density $20.0d_0^{-3}$, resulting in a smooth surface on the inside. The pore is aligned with the x-axis, and the walls extend indefinitely in the y and z axes.

Each of the proteins of interest are attached to a semiflexible polymer composed of 10 beads, with excluded volume interactions. The edge of this polymer is attached to an additional bead through a spring of constant $k_{\mathrm{A}} = 20.0\epsilon/d_0^2$. This bead is pulled at constant velocity, and the spring is then used to measure the force as the translocation takes place. A scheme of this setup is shown in Fig. 9.

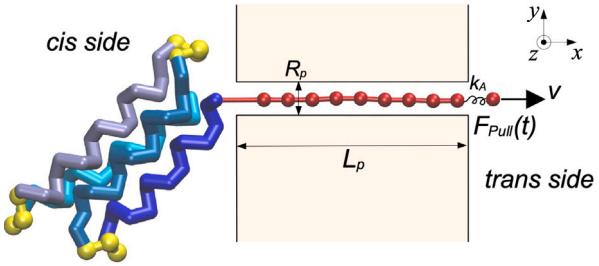

Fig. 9. Schematic depiction of the protein translocation simulations, showing both the 4-α bundle protein and the attached semiflexible polymer. For the protein, the different α-helices are colored in different shades of blue, with the γ-loops in yellow. The semiflexible polymer, of 10 monomers, is attached to one of the extremes of the protein, and is pulled at a constant speed v, measuring in the cantilever spring of elastic constant k_A the pulling force $F_{pull}(t)$.

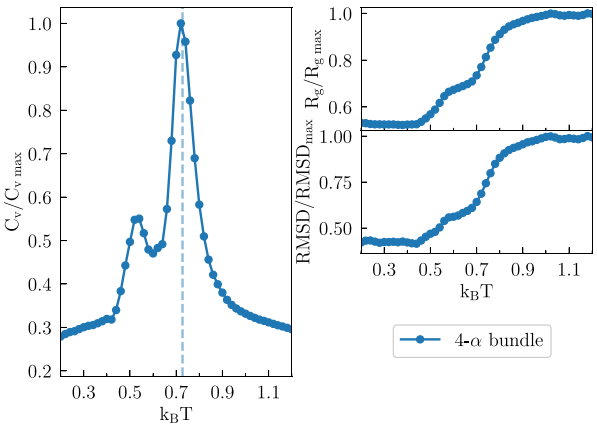

Fig. 10. Left panel: normalized specific heat as a function of the temperature in the thermal simulations for the 4-α bundle. Right panel: normalized radius of gyration and Root Mean Square Deviation (RMSD). The vertical line on the left corresponds to the melting temperature (T_m) obtained from a Gaussian fit around the peak of C_v.

5.1. Integration and units

The whole system is encased in a rectangular box of size 210 × 30 × 30 in units of length d_0, elongated along the x-axis and with periodic boundary conditions. The dynamics of the system are obtained from the integration of its Langevin equation of motion, thus assuming the presence of the solvent implicitly.

For the integration itself the Verlet scheme was taken with $\Delta t = 0.001 t_u$. All of the potentials and constrains of the system were simulated using the software LAMMPS [101], which allows for the construction of coarse-grained Langevin dynamics, and has become increasingly popular in recent years.

Regarding the units of our system, we took d_0, ϵ and m as the units of length, energy and mass respectively, expressing all magnitudes and derivatives in terms of the former, as in Section 2.

The time unit can be derived from the Lennard-Jones timescale, as $t_u = (m d_0^2/\epsilon)^{(1/2)}$, and the unit of force as $F_u = \epsilon/d_0$.

5.2. Thermal stability

As a preparatory study, the thermal stability conditions of the protein has been analyzed, by increasing the temperature of an initial frozen state up to the complete denaturation of the structure. Simulations were carried out on a proteins starting at low temperatures ($k_BT = 0.1\epsilon$). For each of the temperatures, a small thermalization phase to ensure stability and correct starting conditions, and a posterior more extensive production phase have been computed. The transition between temperatures relies on the velocity scaling methods, which consists, at the beginning of each temperature, in the transformation of the velocity distribution of all the particles in the system in the correct form following the Boltzmann distribution. The fingerprint of the denaturation is here the specific heat at constant volume C_v, whose maximum indicates the critical temperature of the transition state in the protein conformation. The results of these simulations are presented in Fig. 10.

The protein denatures at the temperature ($k_BT \approx 0.7\epsilon$), as evidenced by the maximum in the specific heat curve in the left panel of the figure, in agreement with Ref. [94]. The melting temperature was calculated via a Gaussian fit around the peak of C_v, resulting in $T_m = (0.727 \pm 0.002)\epsilon$. The small peak around 0.5ϵ corresponds to a partial unfolding of the protein at its ends, where some of the contacts between beads are broken, making the structure fluctuate at a higher gyration radius (R_g) and higher *Root Mean Square Deviation* (RMSD) with respect to the native structure, as visible in the right panels of Fig. 10. From $T \approx 0.6\epsilon$ onwards, we observe a smaller slope on the two curves, before the final rise towards the saturation value corresponding to the complete denaturation.

5.3. Protein translocation

We show here some preliminary results concerning the secondary structure determination by means of the translocation of one of the proteins of interest, the 4-α bundle.

The temperature used for these simulations is taken in a region that avoids any possible overlap between thermal unfolding events and those caused by the progression of the translocation itself.

Fig. 11 shows the force trajectories measured as the average of the forces recorded in 20 simulations of the translocation, after the alignment of the curves using the time of entrance of the first monomer as trigger. The force F_{pull} is measured through the use of an harmonic cantilever attached to the protein, as described in Fig. 9. The four panels correspond to the different parameters investigated: R_p refers to the radius of the pore, either $1.1 d_0$ (panels A and C) or $1.25 d_0$ (panels B and D), and "Forwards" (panels A and B) and "Reverse" (panels C and D) refer to whether the protein was pulled from the one of its ends or the other.

As the proteins are forced through the pore, the recorded forces change depending on if an α-helix (shadowed in blue) or a γ-loop without structure (shadowed in yellow) is translocating. The curves of Fig. 11 depict a series of peaks corresponding to the translocation of the different regions, with oscillations around a mean value corresponding to the two different structures. To effectively distinguish between the two, a piecewise constant fitting procedure was used, through which the underlying curve was approximated as a series of $N = 7$ discrete force steps. Each of these steps has an associated time domain, and a force value, named F_i, with $i = 1, \ldots, 7$. in our analysis. Both F_i and its correspond domain have been fitted over the real curves, minimizing the mean-squared error. The black curves in Fig. 11 illustrate this fit outcome, showing a very good agreement with the underlying data.

Additionally, to check if α-helices can be effectively distinguished from the γ-loops, the average of the value of force steps belonging to the same structure have been computed, namely $F^\alpha = \sum_{i\in\alpha} F_i$ for α-helices and $F^\gamma = \sum_{i\in\gamma} F_i$ for γ-loops, along with their associated error. These values are reported in Fig. 12 and in Table 4. We notice well differentiated mean values of the force for the two protein regions, but a not completely clear separation if we consider the error bars for the case of pore width $R = 1.1 l_0$, while a more clear separation is obtained for $R = 1.25 l_0$. In any case, the refinement of these outcomes is still in progress with the goal of reducing the fluctuation around the mean values.

It is interesting to note that the advance of the translocation not only affects the force acting on the actual translocating residues, but

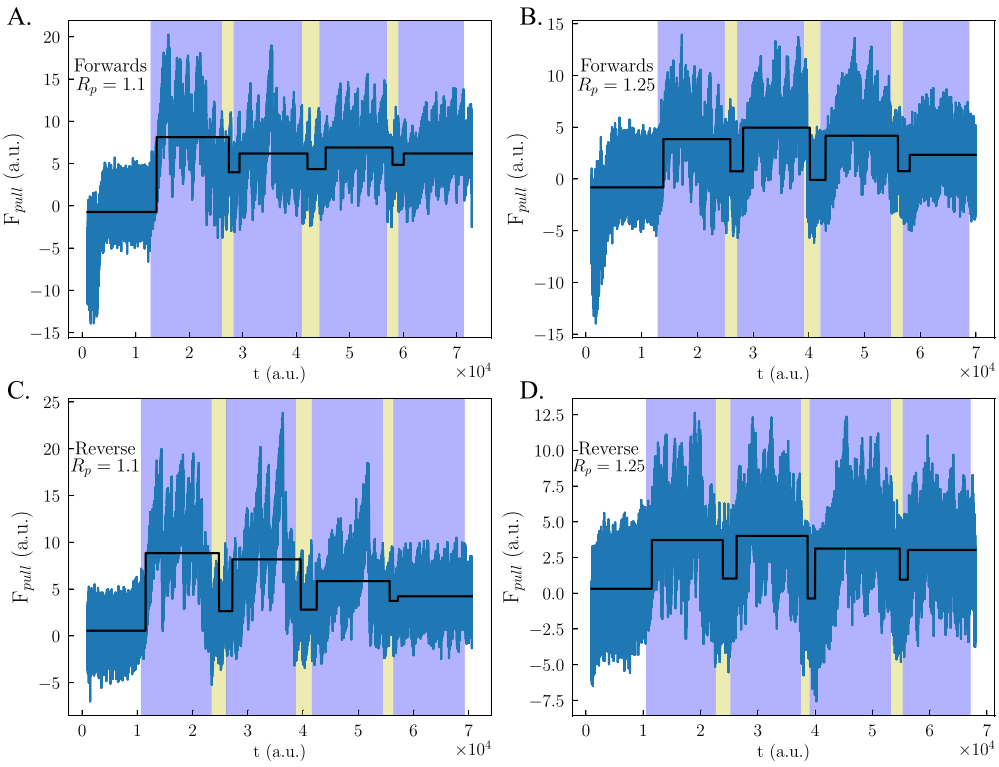

Fig. 11. Force trajectory for the translocation of the protein through two different pore radius ($R_p = 1.1\,d_0$ and $R_p = 1.25\,d_0$) in two different directions (*forward* and *reverse*). These parameters are shown in the top left corner of the corresponding panel. The bands correspond to the α-helix (blue) or a γ-loop (yellow). The fitted force values are shown in black over each image.

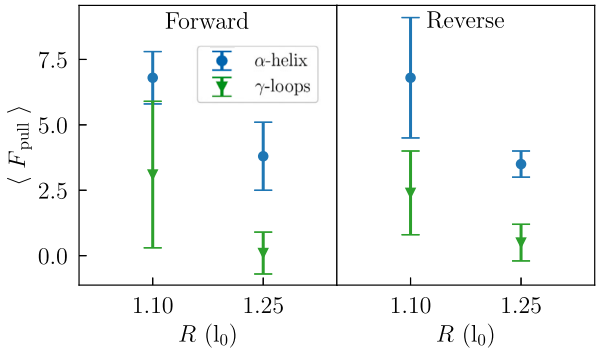

Fig. 12. Pull force $\langle F_{\text{pull}} \rangle$ averaged separately over the substructures α-helices and γ-loops from the values reported in Fig. 11, together with the corresponding error interval, as a function of the pore width R for the two cases: *forward* and *reverse* chain pulling. The values are also displayed in Table 4.

also acts indirectly on the remaining part of the protein still in the *cis*-side of the membrane. In fact, the remaining protein in *cis*-side becomes less stable having already lost elements of protein already translocated, so it tends to denaturate faster than the initial parts, this way requiring a lower force to unfold once passing through the pore. This feature is particularly evident in the fourth blue band of Fig. 11C, which corresponds to the translocation of the last α-helix substructure in the protein.

In more complex molecules the identification of β-sheets, as well as their distinction with respect to the α-helices, are already in progress, and the subject is dedicated to a next study. The outcomes appear at the state very promising, indicating that translocation is a simple and reliable method for the identification of secondary protein structures, without the fine control usually required for voltage-based pore setups.

Table 4
Averaged values of the pull force over the four α-helices (F^α) and the three γ-loops (F^γ) along with their associated errors, fitted over the trajectories of Fig. 11. These values are also plotted in Fig. 12.

R		$F^\alpha \pm \Delta F^\alpha$	$F^\gamma \pm \Delta F^\gamma$
1.1	Forward	6.8 ± 1.0	3.1 ± 2.8
	Reverse	6.8 ± 2.3	0.1 ± 0.8
1.25	Forward	3.8 ± 1.3	2.4 ± 1.6
	Reverse	3.5 ± 1.5	0.5 ± 0.7

6. Summary and conclusions

This review collects the main recent outcomes concerning the time-dependent driven polymer translocation provided by both *pore-driven* and *end-pulled* setups. These approaches can easily be put in connections with experimental polymer translocations, either natural or technological, and provide specific information about the process. Active pore translocation can be modeled as time dependent driving forces spatially distributed in the medium, whereas end-pulled translocation provides a localized application of the driving directly to the molecule edge and permits the analysis of the chain's mechanical response during the process. Altogether, these two approaches with their time dependent features, paint a comprehensive picture of polymer translocation and can reveal optimized aspects of the translocation. One example is represented by the Resonant Activation phenomenon, that addresses the existence of an optimum mean translocation time at a particular frequency range of the driving, depending on polymer size and stiffness. A universal linear relation exists between the optimal mean translocation time with the corresponding sinusoidal driving period in the RA phenomenon, independently on the different parameters involved in the translocation. We have summarized the different scaling behaviors of the mean translocation time with the polymer length, with their relationship with the bending features, and their connection with the free energy potential.

We also study the possibility of describing polymer translocation as a barrier crossing process, topic that, beside the large use in the last years, remains still not totally demonstrated and whose investigation remains open to further exploration.

Finally, we also present preliminary results on the end-pulled translocation of coarse-grained proteins aiming to setup a method able to easily reveal the secondary structures of the molecules. The method, which centers around identifying specific values of the force exerted on a pulling cantilever moving at constant speed for each of the α-helices β-sheets and γ-loops, appears to be a promising effective sequencing procedure based on polymer translocation.

CRediT authorship contribution statement

A. Sáinz-Agost: Writing – review & editing, Writing – original draft, Software, Investigation, Formal analysis, Data curation. **F. Falo:** Writing – review & editing, Validation, Supervision, Funding acquisition, Conceptualization. **A. Fiasconaro:** Writing – review & editing, Validation, Supervision, Formal analysis, Conceptualization.

Declaration of competing interest

The authors declare that they have no known competing financial interests or personal relationships that could have appeared to influence the work reported in this paper.

Acknowledgments

The authors acknowledge the Grant No. PID2020-113582GB-I00 and the Grant No. PID2023-147734NB-I00 funded by MCIN/AEI/10.13039/501100011033, the support of the Aragon Government to the Recognized group 'E36_23R Física Estadística y no-lineal (FENOL)'. A.S-A. also acknowledges the support of the predoctoral FPI fellowship PRE2021-100456 funded by MCIN/AEI/10.13039/501100011033.

Data availability

Data will be made available on request.

References

[1] Kasianowic J, Brandin E, Branton D, Deamer D. Characterization of individual polynucleotide molecules using a membrane channel. Proc Natl Acad Sci 1996;93(24):13770–3.
[2] Lebedev A, Krause M, Isidro A, Vagin A, Orlova E, Turner J, Dodson E, Tavares P, Antson A. Structural framework for DNA translocation via the viral portal protein. EMBO J 2007;26(7):1984–94.
[3] Ishikawa T, Beuron F, Kessel M, Wickner S, Maurizi M, Steven AC. Translocation pathway of protein substrates in clpap protease. Proc Natl Acad Sci 2001;98(8):4328–33.
[4] Schneider G, Dekker C. DNA sequencing with nanopores. Nature Biotechnol 2012;30(4):326–8.
[5] Lee K, Park K, Kim H, Yu J, Chae H, Kim H, Kim K. Recent progress in solid-state nanopores. Adv Mater 2018;30(42):1704680.
[6] Stoloff D, Wanunu M. Recent trends in nanopores for biotechnology. Curr Opin Biotechnol 2013;24(4):699–704.
[7] Choi HS, Ashitate Y, Lee JH, Kim SH, Matsui A, Insin N, Bawendi MG, Semmler-Behnke M, Frangioni JV, Tsuda A. Rapid translocation of nanoparticles from the lung airspaces to the body. Nature Biotechnol 2010;28(12):1300–3.
[8] Muthukumar M. Polymer translocation through a hole. J Chem Phys 1999;111(22):10371–4.
[9] Slonkina E, Kolomeisky AB. Polymer translocation through a long nanopore. J Chem Phys 2003;118(15):7112–8.
[10] Storm AJ, Storm C, Chen J, Zandbergen H, Joanny J-F, Dekker C. Fast DNA translocation through a solid-state nanopore. Nano Lett 2005;5(7):1193–7.
[11] Hamidabad M, Abdolvahab R. Translocation through a narrow pore under a pulling force. Sci Rep 2019;9(1):17885.
[12] Lu L, Wang Z, Shi A, Lu Y, An L. Polymer translocation. Chin J Polym Sci 2023;41(5):683–98.
[13] Schneider G, Kowalczyk S, Calado V, Pandraud G, Zandbergen H, Vandersypen L, Dekker C. DNA translocation through graphene nanopores. Nano Lett 2010;10(8):3163–7.
[14] Hsiao P. Translocation of charged polymers through a nanopore in monovalent and divalent salt solutions: A scaling study exploring over the entire driving force regimes. Polymers 2018;10(11):1229.
[15] Eisenstein M. Oxford nanopore announcement sets sequencing sector abuzz. Nature Biotechnol 2012;30(4):295–6.
[16] Perez-Carrasco R, Fiasconaro A, Falo F, Sancho J. Modeling the mechanochemistry of the ϕ29 DNA translocation motor. Phys Rev E 2013;87(3):032721.
[17] Ait-Haddou R, Herzog W. Brownian Ratchet models of molecular motors. Cell Biochem Biophys 2003;38:191–213.
[18] Fiasconaro A, Mazo J, Falo F. Active polymer translocation in the three-dimensional domain. Phys Rev E 2015;91(2):022113.
[19] Fiasconaro A, Mazo J, Falo F. Translocation time of periodically forced polymer chains. Phys Rev E 2010;82(3):031803.
[20] Cohen J, Chaudhuri A, Golestanian R. Active polymer translocation through flickering pores. Phys Rev Lett 2011;107(23):238102.
[21] Sarabadani J, Ikonen T, Ala-Nissila T. Theory of polymer translocation through a flickering nanopore under an alternating driving force. J Chem Phys 2015;143(7):074905.
[22] Rowghanian P, Grosberg A. Force-driven polymer translocation through a nanopore: An old problem revisited. J Phys Chem B 2011;115(48):14127–35.
[23] Fiasconaro A, Mazo J, Falo F. Translocation of a polymer chain driven by a dichotomous noise. J Stat Mech Theory Exp 2011;2011(11):P11002.
[24] Fiasconaro A, Mazo J, Falo F. Michaelis–Menten dynamics of a polymer chain out of a dichotomous ATP-based motor. New J Phys 2012;14(2):023004.
[25] Fiasconaro A, Mazo J, Falo F. Active translocation of a semiflexible polymer assisted by an ATP-based molecular motor. Sci Rep 2017;7(1):4188.
[26] Sun L, Cao W, Luo M. Free energy landscape for the translocation of polymer through an interacting pore. J Chem Phys 2009;131(19):194904.
[27] Adhikari R, Bhattacharya A. Driven translocation of a semi-flexible chain through a nanopore: A Brownian dynamics simulation study in two dimensions. J Chem Phys 2013;138(20):204909.
[28] Saito T, Sakaue T. Process time distribution of driven polymer transport. Phys Rev E 2012;85(6):061803.
[29] Branton D, Deamer DW, Marziali A, Bayley H, Benner SA, Butler T, Di Ventra M, et al. The potential and challenges of nanopore sequencing. Nature Biotechnol 2008;26(10):1146–53.
[30] Chen K, Jou I, Ermann N, Muthukumar M, Keyser UF, Bell NAW. Dynamics of driven polymer transport through a nanopore. Nat Phys 2021;17(9):1043–9.
[31] Fologea D, Uplinger J, Thomas B, McNabb DS, Li J. Slowing DNA translocation in a solid-state nanopore. Nano Lett 2005;5(9):1734–7.
[32] Noakes MT, Brinkerhoff H, Laszlo AH, Derrington IM, Langford KW, Mount JW, Bowman JL, et al. Increasing the accuracy of nanopore DNA sequencing using a time-varying cross membrane voltage. Nature Biotechnol 2019;37(6):651–6.
[33] Sarabadani J, Ala-Nissila T. Theory of pore-driven and end-pulled polymer translocation dynamics through a nanopore: an overview. J Phys Condens 2018;30(27):274002.
[34] Paun M-A, Paun V-A, Paun V-P. Polymer translocation through nanometer pores. Polymers 2022;14(6):1166.
[35] Neuman K, Nagy A. Single-molecule force spectroscopy: Optical tweezers, magnetic tweezers and atomic force microscopy. Nature Methods 2008;5(6):491–505.
[36] Fiasconaro A, Falo F. Force spectroscopy analysis in polymer translocation. Phys Rev E 2018;98(6):062501.
[37] Ritort F. Single-molecule experiments in biological physics: methods and applications. J Phys: Condens Matter 2006;18(32):R531.
[38] Keyser U, Koeleman B, Dorp S, Krapf D, Smeets R, Lemay S, Dekker N, Dekker C. Direct force measurements on DNA in a solid-state nanopore. Nat Phys 2006;2(7):473–7.
[39] Abdolvahab RH, Ejtehadi MR, Metzler R. Sequence dependence of the binding energy in chaperone-driven polymer translocation through a nanopore. Phys Rev E 2011;83(1):011902.
[40] Adhikari R, Bhattacharya A. Translocation of a semiflexible polymer through a nanopore in the presence of attractive binding particles. Phys Rev E 2015;92(3):032711.
[41] Khalilian H, Sarabadani J, Ala-Nissila T. Polymer translocation in an environment of active rods. Phys Rev Res 2023;5(2):023107.
[42] Khalilian H, Sarabadani J, Ala-Nissila T. Polymer translocation through a nanopore assisted by an environment of active rods. Phys Rev Res 2021;3(1):013080.
[43] Pu M, Jiang H, Hou Z. Polymer translocation through nanopore into active bath. J Chem Phys 2016;145(17):174902.
[44] Sung W, Park P. Polymer translocation through a pore in a membrane. Phys Rev Lett 1996;77(4):783.
[45] Saito T, Sakaue T. Dynamical diagram and scaling in polymer driven translocation. Eur Phys J E 2011;34:1–8.
[46] Dubbeldam J, Rostiashvili V, Milchev A, Vilgis T. Forced translocation of a polymer: Dynamical scaling versus molecular dynamics simulation. Phys Rev E 2012;85(4):041801.

[47] Sun L, Cao W, Luo M. Free energy landscape for the translocation of polymer through an interacting pore. J Chem Phys 2009;131(19):194904.
[48] Muthukumar M. Polymer translocation. CRC Press; 2016.
[49] Menais T. Polymer translocation under a pulling force: Scaling arguments and threshold forces. Phys Rev E 2018;97(2):022501.
[50] Sakaue T. Dynamics of polymer translocation: A short review with an introduction of weakly-driven regime. Polymers 2016;8(12):424.
[51] Sarabadani J, Metzler R, Ala-Nissila T. Driven polymer translocation into a channel: Isoflux tension propagation theory and langevin dynamics simulations. Phys Rev Res 2022;4(3):033003.
[52] Ikonen T, Shin J, Sung W, Ala-Nissila T. Polymer translocation under time-dependent driving forces: Resonant activation induced by attractive polymer-pore interactions. J Chem Phys 2012;136(20):205104.
[53] Doering C, Gadoua J. Resonant activation over a fluctuating barrier. Phys Rev Lett 1992;69(16):2318.
[54] Mantegna RN, Spagnolo B. Experimental investigation of resonant activation. Phys Rev Lett 2000;84(14):3025.
[55] Fiasconaro A, Spagnolo B. Resonant activation in piecewise linear asymmetric potentials. Phys Rev E 2011;83(4):041122.
[56] Pizzolato N, Fiasconaro A, Adorno D, Spagnolo B. Resonant activation in polymer translocation: new insights into the escape dynamics of molecules driven by an oscillating field. Phys Biol 2010;7(3):034001.
[57] Grimaudo R, Valenti D, Spagnolo B, Filatrella G, Guarcello C. Josephson-junction-based axion detection through resonant activation. Phys Rev D 2022;105(3):033007.
[58] Parisi G. Nobel lecture: Multiple equilibria. Rev Modern Phys 2023;95(3):030501.
[59] Sáinz-Agost A, Falo F, Fiasconaro A. Polymer translocation driven by longitudinal and transversal time-dependent end-pulling forces. Phys Rev E 2023;108(3):034501.
[60] Doi M. Introduction to polymer physics. Oxford University Press; 1996.
[61] Luo K, Ala-Nissila T, Ying S-C, Metzler R. Driven polymer translocation through nanopores: Slow-vs.-fast dynamics. EPL (Eur Lett) 2009;88(6):68006.
[62] Hsu H-P, Paul W, Binder K. Estimation of persistence lengths of semiflexible polymers: Insight from simulations. Polym Sci Ser C 2013;55(1):39–59.
[63] Grosberg YA, Nechaev S, Tamm M, Vasilyev O. How long does it take to pull an ideal polymer into a small hole? Phys Rev Lett 2006;96(22):228105.
[64] Luo K, Huopaniemi I, Ala-Nissila T, Ying S-C. Polymer translocation through a nanopore under an applied external field. J Chem Phys 2006;124(11):114704.
[65] Palyulin VV, Ala-Nissila T, Metzler R. Polymer translocation: The first two decades and the recent diversification. Soft Matter 2014;10(45):9016–37.
[66] Sarabadani J, Ikonen T, Ala-Nissila T. Iso-flux tension propagation theory of driven polymer translocation: The role of initial configurations. J Chem Phys 2014;141(21):214907.
[67] Niknam Hamidabad M, Haji Abdolvahab R. Translocation through a narrow pore under a pulling force. Sci Rep 2019;9(1):17885.
[68] Fiasconaro A, Díez-Señorans G, Falo F. End-pulled polymer translocation through a many-body flexible pore. Polym 2022;259:125305.
[69] Huopaniemi I, Luo K, Ala-Nissila T, Ying S-C. Polymer translocation through a nanopore under a pulling force. Phys Rev E 2007;75(6):061912.
[70] Sarabadani J, Ghosh B, Chaudhury S, Ala-Nissila T. Dynamics of end-pulled polymer translocation through a nanopore. EPL (Eur Lett) 2017;120(3):38004.
[71] Mondaini F, Moriconi L. Free energy evaluation in polymer translocation via Jarzynski equality. Phys Lett A 2014;378(26-27):1767–72.
[72] Xue X-G, Zhao L, Lu Z-Y, Li Z-S. Free energy and scalings for polymer translocation through a nanopore: A molecular dynamics simulation study combined with milestoning. Phys Lett A 2012;376(4):290–2.
[73] Valenti D, Denaro G, Adorno D, Pizzolato N, Zammito S, Spagnolo B. Monte Carlo analysis of polymer translocation with deterministic and noisy electric fields. Open Phys 2012;10:560–7.
[74] Pizzolato N, Fiasconaro A, Adorno D, Spagnolo B. Translocation dynamics of a short polymer driven by an oscillating force. J Chem Phys 2013;138(5):054902.
[75] Friddle RW, Noy A, De Yoreo JJ. Interpreting the widespread nonlinear force spectra of intermolecular bonds. Proc Natl Acad Sci 2012;109(34):13573–8.
[76] Kelly SM, Jess TJ, Price NC. How to study proteins by circular dichroism. Biochim Biophys Acta (BBA) - Proteins Proteom 2005;1751(2):119–39.
[77] Barth A. Infrared spectroscopy of proteins. Biochim Biophys Acta (BBA) - Bioenerg 2007;1767(9):1073–101.
[78] Marion D. An introduction to biological NMR spectroscopy. Mol Cell Proteom 2013;12(11):3006–25.
[79] Padlan EA. X-ray crystallography of antibodies. Em Adv Protein Chem 1996;133:57–133.
[80] Srivastava A, Nagai T, Srivastava A, Miyashita O, Tama F. Role of computational methods in going beyond X-ray crystallography to explore protein structure and dynamics. Int J Mol Sci 2018;19(11):3401.
[81] Bai X, McMullan G, Scheres SHW. How cryo-EM is revolutionizing structural biology. Trends Biochem Sci 2015;40(1):49–57.
[82] Asandei A, Di Muccio G, Schiopu I, Mereuta L, Dragomir IS, Chinappi M, Luchian T. Nanopore-based protein sequencing using biopores: Current achievements and open challenges. Small Methods 2020;4(11):1900595.
[83] Li S, Cao C, Yang J, Long Y-T. Detection of peptides with different charges and lengths by using the aerolysin nanopore. ChemElectroChem 2019;6(1):126–9.
[84] Lu Y, Wu X-Y, Ying Y-L, Long Y-T. Simultaneous single-molecule discrimination of cysteine and homocysteine with a protein nanopore. Chem Commun 2019;55(63):9311–4.
[85] Dong Z, Kennedy E, Hokmabadi M, Timp G. Discriminating residue substitutions in a single protein molecule using a sub-nanopore. ACS Nano 2017;11(6):5440–52.
[86] Paul Apurba, Rayabharam Archith, Murkute Punam, Almonte Lisa, Rigo Eveline, Dong Zhuxin, Kumar Ashutosh, Joseph Joshy, Aluru Narayana, Timp Gregory. Decoding proteoforms with single acid resolution using a sub-nanometer diameter pore. bioRxiv 2022. 2022–12.
[87] Nivala J, Marks D, Akeson M. Unfoldase-mediated protein translocation through an α-hemolysin nanopore. Nature Biotechnol 2013;31(3):247–50.
[88] Wei X, Penkauskas T, Reiner JE, Kennard C, Uline MJ, Wang Q, Li S, Aksimentiev A, Robertson JWF, Liu C. Engineering biological nanopore approaches toward protein sequencing. ACS Nano 2023;17(17):16369–95.
[89] Kasianowicz JJ, Robertson JWF, Chan ER, Reiner JE, Stanford VM. Nanoscopic porous sensors. Annu Rev Anal Chem 2008;1(1):737–66.
[90] Luchian T, Park Y, Asandei A, Schiopu I, Mereuta L, Apetrei A. Nanoscale probing of informational polymers with nanopores. Applications to amyloidogenic fragments, peptides, and DNA–PNA hybrids. Acc Chem Res 2019;52(1):267–76.
[91] Sorenson JM, Head-Gordon T. Matching simulation and experiment: A new simplified model for simulating protein folding. J Comput Biol 2000;7(3-4):469–81.
[92] Brown S, Fawzi NJ, Head-Gordon T. Coarse-grained sequences for protein folding and design. Proc Natl Acad Sci 2003;100(19):10712–7.
[93] Bellesia G, Jewett AI, Shea J. Sequence periodicity and secondary structure propensity in model proteins. Protein Sci 19 2010;1(1):141–54.
[94] Guo Z, Thirumalai D. Kinetics and thermodynamics of folding of ade NovoDesigned four-helix bundle protein. J Mol Biol 1996;263(2):323–43.
[95] Rey A, Skolnick J. Computer modeling and folding of four-helix bundles. Proteins: Struct Funct Bioinform 1993;16(1):8–28.
[96] Tapia-Rojo R, Arregui S, Mazo JJ, Falo F. Mechanical unfolding of a simple model protein goes beyond the reach of one-dimensional descriptions. J Chem Phys 2014;141(13):135102.
[97] Tapia-Rojo R, Mazo JJ, Falo F. Thermal versus mechanical unfolding in a model protein. J Chem Phys 2019;151(18):185105.
[98] Honeycutt JD, Thirumalai D. Metastability of the folded states of globular proteins. Proc Natl Acad Sci 1990;87(9):3526–9.
[99] Kar P, Feig M. Recent advances in transferable coarse-grained modeling of proteins. In Adv Protein Chem Struct Biol 2014;96:143–80.
[100] Tozzini V, Rocchia W, McCammon JA. Mapping all-atom models onto one-bead coarse-grained models: General properties and applications to a minimal polypeptide model. J Chem Theory Comput 2006;2(3):667–73.
[101] Thompson AP, Aktulga HM, Berger R, Bolintineanu DS, Brown WM, Crozier PS, In 'T Veld PJ, et al. LAMMPS - a flexible simulation tool for particle-based materials modeling at the atomic, meso, and continuum scales. Comput Phys Comm 2022;271:108171.